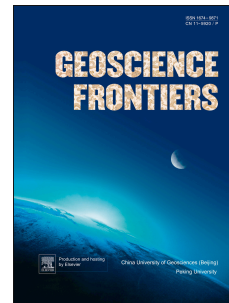


Accepted Manuscript

Zircon U–Pb–Hf constraints from Gongga Shan granites on young crustal melting in eastern Tibet

Nick M.W. Roberts, Michael P. Searle



PII: S1674-9871(18)30072-0

DOI: [10.1016/j.gsf.2018.02.010](https://doi.org/10.1016/j.gsf.2018.02.010)

Reference: GSF 683

To appear in: *Geoscience Frontiers*

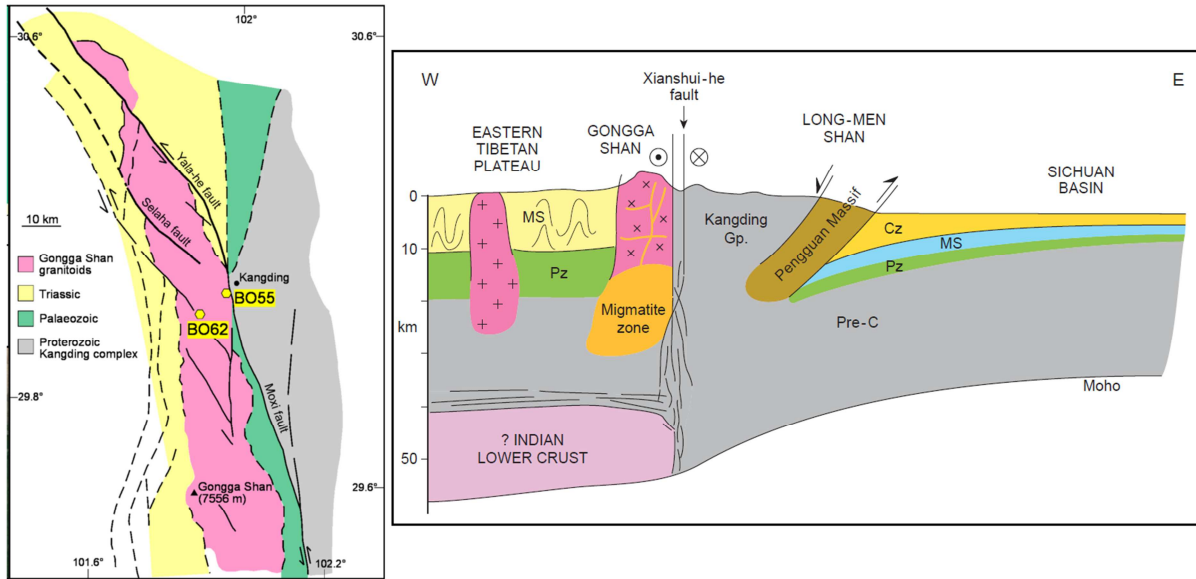
Received Date: 28 June 2017

Revised Date: 21 February 2018

Accepted Date: 27 February 2018

Please cite this article as: Roberts, N.M.W, Searle, M.P, Zircon U–Pb–Hf constraints from Gongga Shan granites on young crustal melting in eastern Tibet, *Geoscience Frontiers* (2018), doi: 10.1016/j.gsf.2018.02.010.

This is a PDF file of an unedited manuscript that has been accepted for publication. As a service to our customers we are providing this early version of the manuscript. The manuscript will undergo copyediting, typesetting, and review of the resulting proof before it is published in its final form. Please note that during the production process errors may be discovered which could affect the content, and all legal disclaimers that apply to the journal pertain.



17 **Abstract**

18 The Gongga Shan batholith is a complex granitoid batholith on the eastern margin of the
19 Tibetan Plateau with a long history of magmatism spanning from the Triassic to the
20 Pliocene. Late Miocene–Pliocene units are the youngest exposed crustal melts within the
21 entire Asian plate of the Tibetan Plateau. Here, we present in-situ zircon Hf isotope
22 constraints on their magmatic source, to aid the understanding of how these young melts
23 were formed and how they were exhumed to the surface. Hf isotope signatures of Eocene
24 to Pliocene zircon rims ($\epsilon_{\text{Hf}}(t) = -4$ to $+4$), interpreted to have grown during localised
25 crustal melting, are indicative of melting of a Neoproterozoic source region, equivalent to
26 the nearby exposed Kangding Complex. Therefore, we suggest that Neoproterozoic crust
27 underlies this region of the Songpan–Ganze terrane, and sourced the intrusive granites that
28 form the Gongga Shan batholith. Localised young melting of Neoproterozoic lower or
29 middle crust requires localised melt-fertile lithologies. We suggest that such melts may be
30 equivalent to seismic and magnetotelluric low-velocity and high-conductivity zones or
31 “bright spots” imaged across much of the Tibetan Plateau. The lack of widespread exposed
32 melts this age is due either to the lack of melt-fertile rocks in the middle crust, the very low
33 erosion level of the Tibetan plateau, or to a lack of mechanism for exhuming such melts.
34 For Gongga Shan, where some melting is younger than nearby thermochronological ages of
35 low temperature cooling, the exact process and timing of exhumation remains enigmatic,
36 but their location away from the Xianshuihe fault precludes the fault acting as a conduit for
37 the young melts. We suggest that underthrusting of dry granulites of the lower Indian crust
38 (Archean shield) this far northeast is a plausible mechanism to explain the uplift and
39 exhumation of the eastern Tibetan Plateau.

40

41 **Keywords:**

42 Tibet; Himalaya; Hf isotopes; Zircon; Crustal melting

43

44

45

46

47 1. Introduction

48 The Himalaya–Tibetan orogen, formed through the collision of India and Asia since ~60–50
49 Ma (Green et al., 2008; Najman et al., 2010, 2017; DeCelles et al., 2014; Hu et al., 2016), is
50 the world’s largest active orogeny, and has greatly contributed to our knowledge of
51 continental collision processes and mountain belt evolution. Continental collision can lead
52 to regional mid- to lower crust metamorphism and crustal melting, and this in turn forms a
53 key part of orogenic evolution, particularly through melt weakening (e.g. Hollister and
54 Crawford, 1986; Rosenberg and Handy, 2005; Jamieson et al., 2011). Orogenic melting in
55 the Himalaya–Tibetan orogen is most exemplified by the leucogranite bodies (Greater
56 Himalaya leucogranites) that stretch the length of the main orogenic belt, forming many of
57 the largest mountain peaks. These Oligocene–Miocene leucogranites are a key aspect of
58 the Himalayan channel flow model (e.g. Hodges, 2000; Searle et al., 2006, 2010; Streule et
59 al., 2010). This model postulates that melt formation in the middle crust in combination
60 with high erosion rates and gravitational instability, enables the exhumation of a channel of
61 melt-weakened middle crust southward towards the Indian foreland (Nelson et al., 1996;
62 Beaumont et al., 2001; Grujic et al., 2002).

63 Elsewhere in the Himalaya–Tibetan orogen, orogenic or post-collisional magmatism
64 is more scattered and can be grouped into four domains: (1) a belt of crustal melts exposed
65 within gneiss domes exposed north of the High Himalaya leucogranites and south of the
66 Indus-Yarlung suture zone (Chen et al., 1990; King et al., 2011; Zeng et al., 2011; Hou et al.,
67 2012); (2) adakitic, potassic and ultrapotassic intrusions and volcanics occurring
68 diachronously across different regions of the Tibetan plateau, and associated with mantle
69 involvement (Miller et al., 1999; Williams et al., 2004; Guo et al., 2006; Chung et al., 2007);
70 (3) localised crustal melts exposed across limited parts of the Tibetan plateau (e.g. Roger et
71 al., 1995; Kapp et al., 2005; Laskowski et al., 2016; Weller et al., 2016; Searle et al., 2016);
72 and (4) “bright spots” imaged in the current middle crust that may represent melting today
73 (Brown et al., 1996; Makovsky et al., 1996; Chen et al., 1996; Wei et al., 2001; Li et al.,
74 2003). The spatial, temporal and geochemically distinct suites of magmatism across the
75 Himalaya–Tibetan orogen provide insight into crustal differentiation and deformation
76 processes during continent collision. This paper examines an example of a localised region
77 of crustal melting near the eastern margin of the Tibetan plateau, known as the Gongga
78 Shan massif. Here we revisit two samples already dated in Searle et al. (2016), presenting

79 new in-situ Hf isotope data from the youngest melts exposed in this long-lived intrusive
80 complex, and we discuss the source and processes behind this very young (Miocene–
81 Pliocene) magmatism.

82

83 **2. Geological setting**

84 Gongga Shan (7556 m) is the highest mountain in the eastern Tibetan Plateau, and is
85 approximately 2.5 km higher than the average elevation of the plateau (Fig. 1). The Gongga
86 Shan massif is mainly composed of a granitoid complex intruded into the Palaeozoic –
87 Triassic sediments of the Songpan–Ganze terrane (SGT) (Fig. 1). The Songpan–Ganze
88 terrane is comprised of a thick sequence of dominantly Triassic flysch-type sediments that
89 were deposited in a branch of Paleotethys, a basin that was inverted during collision
90 between the Qiangtang, and North and South China Blocks (Roger et al., 2010 and
91 references within). The sediments are highly deformed and dominantly folded into tight
92 upright folds (Harrowfield and Wilson, 2005). Deposition occurred from the Late Permian
93 through to the Upper Jurassic, but is mostly Middle–Upper Triassic (e.g. Chen et al., 1995;
94 Bruguier et al., 1997; Weislogel et al., 2010). Provenance has been addressed in several
95 studies, and is from Kunlun and Qinling–Dabie orogens to the north and east, as well as the
96 South China Block and Yidun arc to the east and south (Weislogel et al., 2006, 2010;
97 Enkelmann et al., 2007; Gehrels et al., 2011; Ding et al., 2013; Zhang et al., 2014, 2015). In
98 the east of the SGT, where Gongga Shan is located, the SGT is bound by exposed
99 Neoproterozoic rocks of the Yangtze craton, specifically the ca. 800 Ma Kangding Complex
100 (Zhou et al., 2002; Chen et al., 2005; Zhao et al., 2008). In places the Gongga Shan intrusives
101 are directly in contact with the Kangding Complex, but this boundary forms a strand of the
102 large regional, dominantly strike-slip, left-lateral Xianshuihe fault (Fig. 1c).

103

104 The N–S trending Gongga Shan batholith is over 100 km long but up to only 20 km wide.
105 The outcrop pattern shows how the batholith is clearly cut and offset by strands of the
106 Xianshuihe fault (Fig. 1). These strands shape the Gongga Shan batholith into a left-lateral
107 strike-slip duplex. Field relations show that both ductile and brittle fault exposures cut
108 Gongga Shan granitoids, indicating they both are younger than the magmatism (Searle et
109 al., 2016). Petrologically, the Gongga Shan batholith comprises a wide range of magma
110 types, with both I- and S-type mineral assemblages (Searle et al., 2016). The I-types include

111 biotite and biotite+hornblende monzogranite, granodiorite and granite. The S-types include
112 biotite+tourmaline granite and pegmatite, garnet+muscovite granite, and
113 biotite+muscovite granite. Some outcrops feature evidence of migmatisation of
114 metasedimentary country rocks, with formation of leucogranites. Other outcrops feature
115 enclaves of more mafic magmatic material, which suggest a role of magma mingling in
116 formation of the granitoid suite (Searle et al., 2016).

117
118 Ages for Gongga Shan magmatism can be loosely grouped into four time periods. The
119 earliest group ranges from ca. 216 Ma to 203 Ma, and the second group ranges from ca.
120 182 Ma to 159 Ma (Li et al., 2015; Searle et al., 2016). Some inheritance of the first group is
121 found in the second group. Allantite ages in four 'group one' granitoids at ca. 174–164 Ma
122 indicate thermal reworking of these earlier granitoids during the second period of
123 magmatism, but titanite and allanite ages of ca. 205 Ma in other 'group one' granitoids
124 suggest that the ca. 182–159 Ma tectono-thermal activity was not pervasive. The third
125 group of granitoids is poorly constrained. It comprises: (1) a pegmatite with populations of
126 zircon ages at 41 Ma (Searle et al., 2016); (2) a migmatitic granite with two zircon ages at
127 ca. 35 Ma (Searle et al., 2016); (3) a migmatite with zircon populations in the leucosome
128 and melanosome at ca. 32 and 27 Ma respectively (Li and Zhang, 2013). The fourth group
129 ranges from 18 Ma to 4 Ma (Roger et al., 1995; Liu et al., 2006; Li and Zhang, 2013; Li et al.,
130 2015; Searle et al., 2016; Zhang et al., 2017), and also includes allanite ages of 16–5 Ma
131 (Searle et al., 2016).

132
133 The tectonic setting during each of the magmatic periods forming the Gongga Shan
134 batholith is poorly constrained. To our knowledge there is no published geochemical study
135 that may help in this regard. Roger et al. (1995) provided some limited whole-rock
136 geochemistry and Pb–Pb, Rb–Sr and Sm–Nd isotopic data, but only one of their samples
137 received combined U–Pb and isotopic analysis, which is requisite in such a complex
138 granitoid complex. Their data provide Nd model ages ranging from 1.49 Ga to 1.24 Ga.
139 Searle et al. (2016) suggested an Andean-type setting during the 215–159 Ma periods of
140 magmatism, although they did not provide specific lines of evidence for this interpretation.
141 This setting would fit the range of I- and S-type lithologies and the protracted nature of the
142 magmatic episodes. The young periods of magmatism are inferred to be related to crustal

143 melting (Roger et al., 1995; Searle et al., 2016), and overlap with on-going convergence in
144 the Himalaya–Tibetan orogen. Li and Zhang (2013) postulated that migmatisation may be
145 related to activity along the Xianshuihe fault zone, but field observations along the Gongga
146 Shan batholith show that the strike-slip faults cut relatively undeformed granite, indicating
147 that faulting post-dated the adjacent granites (Searle et al., 2016).

148

149 **3. Samples**

150 *3.1 BO55*

151 BO55 is an undeformed pegmatitic granite from Shuguang Bridge that cuts across both an
152 earlier biotite monzogranite, which has a weak foliation, and a more leucocratic biotite-
153 muscovite granite that exhibits partial melt structures (schlieren of melanosomes). The
154 migmatitic granite itself intrudes the monzogranite. U–Pb geochronology yielded four old
155 analyses at 159 ± 4 Ma, populations at 41 Ma and 37 Ma and younger dates spreading from
156 22 Ma to 15 Ma, possibly representing lead-loss, to 15 Ma or even younger (Searle et al.,
157 2016). Allanite yielded two populations of U–Pb age data, one at ca. 173 Ma and one at ca.
158 15 Ma. The overlap between the allanite age and the youngest zircon led Searle et al.
159 (2016) to suggest the intrusion age was 15 Ma.

160

161 *3.2 BO62*

162 BO62 is a biotite monzogranite from the middle part of the batholith that is cut by later,
163 minor intrusions of biotite-tourmaline pegmatites and muscovite-garnet granite veins. U–
164 Pb age data (Searle et al., 2016) yielded a strong mixing line between ca. 800 Ma and a
165 Neogene lower intercept. The younger analyses reveal concordant populations at both ca.
166 14 Ma, and ca. 6–5 Ma. An imprecise allanite lower intercept age of 5 Ma was also
167 determined. Searle et al. (2016) interpreted the data to represent crystallisation of melt at
168 ca. 5 Ma.

169

170 **4. Method**

171 Lu–Hf isotopes were measured at the NERC Isotope Geosciences Laboratory (Nottingham,
172 UK) using a Thermo Scientific Neptune Plus multi-collector inductively coupled mass
173 spectrometer (ICP-MS) coupled to a New Wave Research 193UC excimer laser ablation
174 system fitted with a TV2 cell. He carrier gas was added to Ar sourced from Cetac Aridus II

175 desolvating nebuliser at a Y-piece before entering the torch. Ablation conditions were 30
176 μm spots at 10 Hz and a fluence of 6.5 J/cm^2 , measured for 30 s. The spots were placed
177 directly over pits previously analysed for U–Pb (presented in Searle et al., 2016). Masses
178 measured are ^{172}Yb , ^{173}Yb , ^{175}Lu , $^{176}\text{Hf}+\text{Yb}+\text{Lu}$, ^{177}Hf , ^{178}Hf , ^{179}Hf and ^{180}Hf . A standard–
179 sample–standard bracketing technique using reference zircon 91500 (Wiedenbeck et al.,
180 1995, 2004) was used to correct $^{176}\text{Lu}/^{177}\text{Hf}$ and $^{176}\text{Hf}/^{177}\text{Hf}$ ratios. Plešovice (Sláma et al.,
181 2008) and the synthetic zircon MUNZirc (Fisher et al., 2011) were used to monitor accuracy
182 and precision of internally corrected Lu and Hf isotope ratios. The reference solution
183 JMC475 was analysed at the start of each analytical session as both undoped and doped
184 with 50 ppb Yb. The correction for ^{176}Yb on the ^{176}Hf peak was made using reverse-mass-
185 bias correction of the $^{176}\text{Yb}/^{173}\text{Yb}$ ratio (0.7941), after empirical derivation using the Hf
186 mass bias corrected Yb-doped JMC475 solution measurements (Nowell and Parrish, 2001).
187 The ^{176}Lu interference on the ^{176}Hf peak was corrected by using the measured ^{175}Lu and
188 natural $^{176}\text{Lu}/^{175}\text{Lu}$ ratio (0.02653) and assuming a mass bias equivalent to Hf. The
189 reproducibility of the $^{176}\text{Lu}/^{177}\text{Hf}$ and $^{176}\text{Hf}/^{177}\text{Hf}$ measurements of 91500 was
190 approximately 0.45 and 0.01 % (2s) respectively. The secondary reference material
191 Plešovice gave a weighted mean $^{176}\text{Hf}/^{177}\text{Hf}$ ratio of 0.282468 ± 0.000024
192 (0.282482 ± 0.000013 ; Sláma et al., 2008), and MUNZirc gave 0.282156 ± 0.000026
193 (0.282135 ; Fisher et al., 2011). Calculation of age-corrected initial $^{176}\text{Hf}/^{177}\text{Hf}$ ratios used
194 the decay constant of Söderlund et al. (2004), the CHUR value of Bouvier et al., (2008), and
195 are reported as $\epsilon_{\text{Hf}}(t)$. Data were screened using the ablation signal profiles so that
196 ablations with mixed age domains were excluded.

197

198 5. Results

199 5.1 BO55

200 Nine analyses were made across nine grains (Fig. 2), with the analyses spread across all age
201 domains in the sample. The four Miocene age domains have $\epsilon_{\text{Hf}}(t)$ values ranging from –
202 4.12 to –2.02 (Fig. 3). The three ca. 40 Ma age domains have $\epsilon_{\text{Hf}}(t)$ values of –1.92 to +1.60,
203 and the two Triassic inherited cores have $\epsilon_{\text{Hf}}(t)$ of –2.01 and –0.71. Figure 3 shows $\epsilon_{\text{Hf}}(t)$
204 plotted versus apparent ($^{206}\text{Pb}/^{238}\text{U}$) age. Lu–Hf evolution trends for zircon lead-loss (Lu–Hf
205 = 0) and the evolution of an average crustal composition (Lu/Hf = 0.015; Griffin et al., 2002)
206 are shown for comparison.

207

208 *5.2 BO62*

209 Twenty-six analyses were made across nineteen grains (Fig. 2). Of these, eleven correlate
210 with ca. 800 Ma inherited cores, eight correlate with ca. 5 Ma rims, one correlates with a
211 ca. 14 Ma rim, and the other five represent mixtures between these (Fig. 3). The $\epsilon_{\text{Hf}}(t)$
212 values (Fig. 3) of the 5 Ma rims ranges from -1.90 to $+3.64$, and the $\epsilon_{\text{Hf}}(t)$ values of the 800
213 Ma cores ranges from $+5.16$ to $+10.10$. The analyses that represent age mixtures, probably
214 due to the spots overlapping different age domains, feature $\epsilon_{\text{Hf}}(t)$ signatures that are
215 compatible with physical mixing between the ca. 800 core and ca. 5 Ma rim ages.

216

217 **6. Discussion**218 *6.1 Magma source*

219 The $\epsilon_{\text{Hf}}(t)$ values of the ca. 14–5 Ma rims on BO62 do not fall on a line lead-loss trajectory
220 (i.e. $\text{Lu}-\text{Hf} = 0$) from the ca. 800 Ma core $\epsilon_{\text{Hf}}(t)$ values (Fig. 3). This confirms the conclusion
221 of Searle et al. (2016) that the rims represent new zircon crystallisation and/or dissolution-
222 re-precipitation in the presence of melt. The fact that these rim $\epsilon_{\text{Hf}}(t)$ signatures fall on a
223 trajectory representing the evolution of average upper continental crust (i.e. $\text{Lu}-\text{Hf} =$
224 0.015), is compatible with reworking of the 800 Ma source rock without addition of
225 material significantly more juvenile, such as depleted mantle. The signatures of BO55
226 overlap those of BO62, suggesting a similar magmatic source; this is apparent for both the
227 ca. 41 Ma and ca. 17 Ma rim domains. The $\epsilon_{\text{Hf}}(t)$ signature of the two Triassic zircon
228 domains overlaps the broad evolution of the potential ca. 800 Ma source, suggesting that
229 the inherited magmatic rock in BO55 may also be derived from this Neoproterozoic source.

230

231 The $\epsilon_{\text{Hf}}(t)$ signature of potential source rocks is shown in Fig. 3b. The Neoproterozoic cores
232 in BO62 overlap directly with values from the similarly aged Kangding Complex that is
233 exposed to the east of the Gongga Shan batholith (Fig. 1). This provides strong evidence
234 that BO62 is derived from remelting of Kangding Complex crust, or a source region that also
235 produced this Neoproterozoic magmatic province. The Kangding Complex broadly overlaps
236 other late Neoproterozoic magmatic rocks that are found throughout the west and
237 northern borders of the Yangtze cratonic margin. There is limited $\epsilon_{\text{Hf}}(t)$ data on other
238 granitoids that intrude the Songpan–Ganze terrane; the two Triassic analyses from Gongga

239 Shan overlap these, implying a possible similarity in magmatic source, but there is also
240 considerable spread in the other granitoids. The Triassic sedimentary rocks that form the
241 cover of the Songpan–Ganze terrane have a wide range in $\epsilon_{\text{Hf}}(t)$ values, and a broad range of
242 Palaeozoic to Mesozoic ages. If these sedimentary signatures were averaged together, then
243 their isotopic signature would overlap that of the Triassic and Oligocene–Miocene zircon
244 domains in the Gongga Shan rocks. Whether this is likely will be discussed in the next
245 section.

246
247 The $\epsilon_{\text{Nd}}(t)$ signature of the rock suites shown in Fig. 3a–c. The plot shows that the SGT
248 granitoids are compatible with reworking of a Neoproterozoic source region, as seen in the
249 Hf plot, and the same applies to the Gongga Shan data. It should be noted that these latter
250 data are not all directly dated, and plotted at the 12 Ma intrusion age that is reported by
251 Roger et al. (1995). Interestingly, the SGT sediments have a much more limited range in
252 $\epsilon_{\text{Nd}}(t)$ space than $\epsilon_{\text{Hf}}(t)$, and are distinctly more evolved than both the SGT granitoids and the
253 Gongga Shan rocks.

254

255 *6.2 Melting of Neoproterozoic basement*

256 The distinct $\epsilon_{\text{Nd}}(t)$ and $\epsilon_{\text{Hf}}(t)$ signature of the Miocene Gongga Shan magmatic rocks
257 indicates that the Triassic SGT sediments that they intrude are not the most likely source,
258 this in fact corresponds to a Neoproterozoic source, represented by the nearby Kangding
259 Complex. Zircon inheritance data can be used to investigate this more thoroughly. A plot
260 showing both all published magmatic crystallisation ages and all published in-situ zircon
261 spot ages from Gongga Shan is shown in Fig. 4. It is clear that there is very little inheritance
262 of Palaeozoic to Triassic ages that are dominant in the SGT flysch-type sediments (Wieslogel
263 et al., 2006, 2010; Zhang et al., 2014, 2015). Searle et al. (2016) inferred that the Gongga
264 Shan intrusions were sourced from melting of this Triassic sedimentary fill, this is because
265 these rocks would have been fertile (i.e. mica-rich) allowing for partial melt formation at
266 moderate temperatures. Production of granitoids from melting of the Triassic SGT is one of
267 the models inferred for granitoids found elsewhere across the SGT (Roger et al., 2004,
268 2010). This particularly accounts for the S-type nature of many of the granites, although it
269 does not clearly explain the existence of several A- and I-types (Roger et al., 2004; Zhang et
270 al., 2006, 2007; Xiao et al., 2007; Weislogel, 2008; Searle et al., 2016).

271

272 If we accept a Neoproterozoic source for the Gongga Shan granites as the data imply, then
273 firstly we can infer that Neoproterozoic (Yangtze margin) crust underlies the region of the
274 Gongga Shan batholith. The basement to the SGT has been debated (Roger et al., 2010 and
275 references within), but is inferred by Roger et al. (2010) to be Neoproterozoic crust similar
276 to the Yangtze craton, on the eastern edge of the SGT (Zhou et al., 2002). Gongga Shan,
277 also located on the eastern border of the SGT, supports this model at least for the southern
278 part of the SGT. The reason for melting of this Neoproterozoic crust remains enigmatic
279 however. The Triassic–Jurassic intrusions may be related to: (1) crustal thickening and
280 burial during the Indosinian orogeny (Roger et al., 2004, 2010); (2) a slab tear from
281 opposing subduction zones either side of the SGT (de Sigoyer et al., 2014); (3) post-
282 collisional delamination (Zhang et al., 2007); or (4) tearing of the thickened lower crust
283 after infilling of the sedimentary basin (Yuan et al., 2010). The Oligocene–Miocene melts
284 imply that over 100 Myrs later, during the on-going Himalaya–Tibetan orogeny, that the
285 magmatic source region was reactivated or that new (but isotopically similar) source
286 regions were partially melted; both possibilities may have involved decompression melting
287 as a potential mechanism.

288

289 There is no clear surface geological evidence for Cenozoic metamorphism in the Gongga
290 Shan region, or in fact the SGT as a whole. The deformation observed in the SGT
291 sedimentary cover is inferred to be largely Indosinian (Harrowfield and Wilson, 2005).
292 Weller et al., (2013) dated Barrovian burial metamorphism in the Danba region to the NE of
293 Gongga Shan at 192 Ma (Staurolite-grade) to 174 Ma (Sillimanite-grade). Their study
294 constrained what was previously thought to be a mixture of tectonothermal events based
295 on scattered metamorphic ages (Hou et al., 1996; Huang et al., 2003a, b). Airaghi et al.
296 (2017) identified an Early Jurassic greenschist metamorphism in the Pengguan massif along
297 the Beichuan fault (Longmen Shan Fault Zone) at 140–135 Ma, which they argue is the
298 onset of thick-skinned deformation in that region. Young movement within the Longmen
299 Shan Fault Zone is known from the $M=8$ 2008 Wenchuan earthquake and other smaller
300 more recent movements (Hubbard and Shaw, 2008; Wang et al., 2014). Active deformation
301 here is localised as steep faults that form a thick-skinned fold and thrust belt bounding the
302 Sichuan Basin to the east (Hubbard et al., 2010; Li et al., 2010, 2014). This lack of

303 widespread Cenozoic deformation and metamorphism in the SGT is in contrast to the south
304 Tibetan margin, where the High Himalaya expose high-grade metamorphic rocks exhumed
305 from the mid-crust, that are associated with large volumes of partial melt (see Searle et al.,
306 2010; Cottle et al., 2015).

307

308 *6.3 Comparison to other young melts*

309 Gongga Shan does not represent the only young crustal melt in the Asian plate rocks of the
310 Tibetan Plateau that is now exposed at the surface. Shown on Fig. 1b are three other
311 known localities. The Western Nyainqentanglha mountains in the Lhasa terrane of
312 Southern Tibet reveals distinct similarities to the Gongga Shan massif. Nyainqentanglha
313 comprises sediments metamorphosed in the Triassic, which have been intruded by
314 granitoids over a protracted history, ranging in age from ca. 213 Ma to 8 Ma (Xu et al.,
315 1985; Liu et al., 2004; Kapp et al., 2005; Weller et al., 2016). The magmatic rocks were
316 exhumed from the mid-crust (ca. 15–20 km depth) since the late Neogene (Armijo et al.,
317 1985; Harrison et al., 1995). The Lunggar Rift in south-west Tibet features granitoids
318 formed between ca. 22 Ma and 8 Ma (Kapp et al., 2008). In Ulugh Muztagh, north Tibet,
319 leucogranites formed at shallow levels (ca. 10 km) between ca. 10 Ma and 8 Ma, and
320 intrude into Triassic sandstone (Burchfiel et al., 1989).

321

322 These crustal melt leucogranites located sporadically across the Asian plate side of the
323 suture zone in Tibet are not the same as the Indian plate leucogranites, exposed along the
324 Greater Himalaya (Searle et al., 2010) or the Yarlung suture zone (Laskowski et al., 2017).
325 The Greater Himalayan Sequence (GHS) leucogranites are sourced and intruded into Indian
326 plate rocks south of the suture zone. They are in situ melts from kyanite or silimanite ±
327 cordierite migmatites and intruded as a vast network of sills and dykes in the GHS. The
328 Tibetan leucogranites (although of similar age as the younger GHS melts) are different; they
329 are melts derived from and intruded into rocks of the over-riding Asian plate, their source is
330 deeper and generally not exposed, their geochemistry and isotopes distinctly different from
331 the GHS, and they intrude older rocks of, for example, the Lhasa block. The Gongga Shan
332 leucogranites are located much further north across at least another plate boundary
333 (Bangong suture zone) and possibly yet another (Jinsha suture), and separated by hundreds
334 of km where they are no known exposed Cenozoic leucogranites.

335

336 Weller et al. (2016) suggested that Nyainqentanglha, and by inference the other regions of
337 young exposed crustal melting, may be exhumed examples of localised mid-crustal partial
338 melts that can be seen in the middle crust of Tibet today as seismic - magnetotelluric
339 'bright spots'. These bright spots, recorded by INDEPTH seismic data (e.g. Brown et al.,
340 1996; Makovsky et al., 1996; Wei et al., 2001), represent either melt or fluid (Makovsky and
341 Klemperer, 1999; Unsworth et al., 2005), but either way, imply the existence of pockets of
342 melt in the middle crust (Gaillard et al., 2004). Weller et al. (2016) suggested that their
343 localisation is directly related to the existence of melt-fertile source rocks. This is intriguing
344 given the case of Gongga Shan, where Neoproterozoic crust is inferred to be the magmatic
345 source according to the present study. The melts forming the Gongga Shan leucogranites
346 suggest that this Neoproterozoic 'basement' must comprise melt-fertile metasedimentary
347 or meta-igneous units. The fact that young melts such as the Gongga Shan leucogranites
348 are rarely seen in Asian plate rocks across the Tibetan plateau, is either due to the lack of
349 melt-fertile rocks within the mid-crust, and/or to the lack of mechanisms to exhume and
350 expose the crustal melts after they have formed. It may be that melt-fertile rocks produce
351 melt during earlier stages of collisional orogeny, and that fertile regions remain scarce by
352 late stages of orogeny. Both the Lunggar Rift and Nyainqentanglha, which is associated with
353 the Yadong-Gulu Rift, are characterised by upper crustal extensional faulting, and hence,
354 this could provide a mechanism to exhume the exposed melts (Kapp et al., 2008; Weller et
355 al., 2016). However, the distribution of leucogranites away from the shallow normal faults
356 that appear to cut them, suggests no direct link between Cenozoic upper crustal extension
357 and crustal melting (Searle et al., 2011).

358

359 *6.4 Exhuming Gongga Shan*

360 Whereas the Lunggar Rift and Nyainqentanglha granitoids are associated with extensional
361 rifts, the Gongga Shan batholith appears to be associated with the Xianshuihe strike-slip
362 fault. This regional scale fault system, which features a series of onlapping strands as it
363 transects the Gongga Shan batholith (see Fig. 1), cuts across all intrusions (Searle et al.,
364 2016). Li and Zhang (2013) related Oligocene migmatisation in Gongga Shan to an earlier
365 phase of movement, but it is not clear how the observed ductile fabric is related to the
366 cross-cutting brittle fabric. Roger et al. (1995) inferred that the 12.8 Ma age they obtained

367 for a Gongga Shan granite provided the age of onset of movement for the Xianshuihe fault.
368 Searle et al. (2016) lowered this age to ca. 5 Ma, based on their youngest magmatic age.
369 Recently, Zhang et al. (2017) provided another very young age from a similar part of the
370 batholith at ca. 4 Ma, providing further confirmation of Pliocene magmatism.

371
372 The uplift history of Gongga Shan has been estimated by a range of techniques, comprising
373 Rb–Sr, Ar–Ar and zircon and apatite fission tracks ages, most recently synthesised in Zhang
374 et al. (2017). In their combined zircon and apatite fission track-based study, Zhang et al.
375 (2017) interpreted their data as recording rapid uplift commencing at 9 Ma, and slowing
376 down since 4 Ma. Regionally, thermochronology has shown that the southeast Tibetan
377 plateau (exclusive of the Namche Barwa syntaxis) has experienced little rock uplift and
378 erosion since the Cretaceous (Lai et al., 2007; Zhang et al., 2017). The thermochronological
379 data are interesting considering the geochronological ages of magmatism. They suggest
380 that melting, presumably of the middle crust given the inferred Neoproterozoic source,
381 occurred both shortly before, and after, rapid exhumation of the massif. Zhang et al. (2017)
382 also suggested that movement of the northern Yalaha strand of the Xianshuihe fault zone
383 was active between 9 Ma and 4 Ma, i.e. before the youngest melts intruded.

384
385 In summary, we envisage the large-scale crustal structure in Fig. 5. Both Triassic and
386 younger Gongga Shan components are presumed to be derived from Neoproterozoic
387 source rocks underlying the region. The Triassic magmatism broadly overlapped and
388 followed regional Indosinian deformation of the Songpan–Ganze sediments (e.g.
389 Harrowfield and Wilson, 2005; Roger et al., 2010). Precambrian rocks crop out at the
390 surface in eastern Tibet (Kangding complex) above crust possibly as thick as 60–65 km
391 (Nabelek et al., 2009). This great thickness of Precambrian is best explained by Argand-type
392 underplating of lower Indian crust beneath the south and central part of Tibet (Searle et al.,
393 2011). The young Cenozoic melts intruding the older components of the Gongga Shan
394 batholith were all uplifted by transpressional deformation associated with left-lateral
395 strike-slip shearing along the Xianshuihe fault. Zhang et al. (2017) proposed that rapid
396 exhumation started in the north of the batholith at ~9 Ma and slowed down since ~4 Ma.
397 Our data suggest that young leucogranites occur along the eastern side of the batholith
398 adjacent to the fault which cuts them, and hence we infer that rapid exhumation occurred

399 since 5–4 Ma, whilst the surrounding plateau maintained its already ~ 5 km high elevation.
400 Many of the Pliocene granites in Gongga Shan have younger crystallisation ages than the
401 low-temperature thermochronological ages in the surrounding parts of the plateau (Zhang
402 et al., 2017).

403
404 Surface- and body-wave tomography indicate that all of southern Tibet is underlain by high-
405 velocity Indian crust (Preistley et al. 2008). Thermal models, combined with experimentally-
406 derived flow laws suggest that if the Indian lower crust is anhydrous, it will remain strong as
407 it progressively underplates the southern part of Tibet during convergence. Based on
408 earthquake observations and thermal models, Craig et al. (2012) proposed that the 600 °C
409 isotherm (the highest temperature cut-off for earthquakes) could extend horizontally for
410 450–500 km beneath the Tibetan plateau. Gongga Shan is approximately 350 km NE of the
411 Eastern Himalayan syntaxis of definite Indian crustal origin. Searle et al. (2016) postulated
412 that underthrust lower Indian crust (dry Archean granulites) could have extended as far
413 northeast as the Xianshuihe fault under eastern Tibet, and that this underthrusting and
414 overthickening of the crust could explain the localised young mid-crustal melting at Gongga
415 Shan (Fig. 5). The melt source for the young Cenozoic Gongga Shan leucogranites would lie
416 in the mid-crust, the Asian plate Proterozoic basement gneisses above the lowermost crust
417 comprised of Indian Shield-derived granulites (Fig. 5).

418

419

420

421 **7. Conclusions**

422 The source of young (ca. 15–4 Ma) crustal melts exposed in the Gongga Shan batholith,
423 along the eastern margin of the Tibetan plateau, is interpreted to be Neoproterozoic crust
424 equivalent to the adjacent Kangding Complex. This crust underlies the thick Triassic
425 Songpan–Ganze sedimentary package locally, and perhaps across the region. Young melts
426 require melt-fertile rocks, which may be sparse at this late stage of the collisional orogeny.
427 The melts may be exhumed equivalents to the seismic – magnetotelluric “bright spots”
428 imaged under other parts of the Tibetan Plateau. The process of their formation in this part
429 of eastern Tibet remains enigmatic, although decompression melting is a plausible
430 mechanism. Data shows that uplift is coincident with the latest magmatism, and it is

431 inferred that regional structures play a role in exhumation. Underthrusting of India, rather
432 than lower crustal flow, is one mechanism to uplift the region at this stage of the ongoing
433 Himalayan-Tibetan orogeny. The final stage of exhumation of the Gongga Shan batholith
434 with its young leucogranites was likely a result of transpression along the curved restraining
435 bend of the dextral Xianshuihe strike-slip fault.

436

437

438 **Acknowledgements**

439 We thank the Institute of Geology, China Earthquake Administration, Beijing for assistance
440 in the field. NR publishes with permission of the Executive Director of the British Geological
441 Survey, UK.

442

443

444 **Figure Captions**

445 Figure 1. (a) Sketch map of central Asia showing terranes involved in the Himalaya–Tibetan
446 orogeny. (b) Satellite image (Google Earth™) of the Tibetan Plateau showing locations
447 referred to in the text. (c) Simplified geological map of the Gongga Shan batholith and
448 major structures of the Xianshuihe fault, after Searle et al. (2016).

449
450 Figure 2. Cathodoluminescence images of selected zircons from samples BO55 and BO62,
451 showing location of spots for Hf isotope analysis.

452
453 Figure 3. (a) $\epsilon_{\text{Hf}}(t)$ vs. zircon age ($^{206}\text{Pb}/^{238}\text{U}$; Ma) for individual spot analyses, this study. (b)
454 $\epsilon_{\text{Hf}}(t)$ data for this study compared to potential source regions – Songpan–Ganze sediments
455 (Zhang et al., 2014, 2015), Songpan–Ganze granitoids (Cai et al., 2009, 2010), Yangtze
456 margin (Zheng et al., 2007; Zhao et al., 2008a,b; Wang et al., 2012), Kangding (Zheng et al.,
457 2007). (c) $\epsilon_{\text{Nd}}(t)$ vs. Age (Ma) for the Gongga Shan granitoids (Roger et al., 1995) compared
458 to potential source regions - Songpan–Ganze sediments (Chen et al., 2007; de Sigoyer et al.,
459 2014), Songpan–Ganze granitoids (Roger et al., 2004; Xiao et al., 2007; Zhang et al., 2007;
460 Cai et al., 2009, 2010; Yuan et al., 2010; de Sigoyer et al., 2014), Yangtze margin (Zhou et
461 al., 2006; Zhao and Zhou 2007a, b; Chen et al., 2015).

462
463 Figure 4. (a) Probability density plot of U–Pb detrital zircon ages from the southern portion
464 of the Songpan–Ganze terrane (Weislogel et al., 2006, 2010; Zhang et al., 2014). (b)
465 Probability density plot of U–Pb zircon spot ages for concordant (<10%) spot analyses from
466 Gongga Shan (Li and Zhang, 2013; Li et al., 2015; Searle et al., 2016; Zhang et al., 2017). (c)
467 Probability density plot of all U–Pb zircon magmatic ages from Gongga Shan (Roger et al.,
468 1995; Liu et al., 2006; Li and Zhang, 2013; Li et al., 2015; Searle et al., 2016; Zhang et al.,
469 2017).

470
471 Figure 5. Sketch cross-section of a composite eastern Tibet – Gongga Shan – Sichuan basin
472 profile showing crustal structure. In our speculative model, the lowermost crust is
473 composed of underthrust Indian lower crust (Archaean granite). Triassic granites intrude
474 the Palaeozoic–early Mesozoic sedimentary cover of eastern Tibet. Precambrian rocks crop
475 out in eastern Tibet (Pengguan massif). The source for crustal melting in Gongga Shan is the

476 Proterozoic mid-crust of Tibet. The eastern margin of the plateau is marked by the Long-
477 Men Shan range, and steep-west-dipping thrust faults overthrusting the western margin of
478 the Sichuan basin.

479

480

481 **References**

482

483 1. Airaghi, L., de Sigoyer, J., Lanari, P., Guillot, S., Vidal, O., Monié, P., Sautter, B. and
484 Tan, X., 2017. Total exhumation across the Beichuan fault in the Longmen Shan (eastern
485 Tibetan plateau, China): Constraints from petrology and thermobarometry. *Journal of Asian*
486 *Earth Sciences*, 140, 108-121.

487

488 2. Armijo, R., Tapponnier, P., Mercier, J.L. and Han, T.L., 1986. Quaternary extension in
489 southern Tibet: Field observations and tectonic implications. *Journal of Geophysical*
490 *Research: Solid Earth*, 91, 13803-13872.

491

492 3. Beaumont, C., Jamieson, R.A., Nguyen, M.H. and Lee, B., 2001. Himalayan tectonics
493 explained by extrusion of a low-viscosity crustal channel coupled to focused surface
494 denudation. *Nature*, 414, 738-742.

495

496 4. Bouvier, A., Vervoort, J.D. and Patchett, P.J., 2008. The Lu–Hf and Sm–Nd isotopic
497 composition of CHUR: constraints from unequilibrated chondrites and implications for the
498 bulk composition of terrestrial planets. *Earth and Planetary Science Letters*, 273, 48-57.

499

500 5. Bruguier, O., Lancelot, J.R. and Malavieille, J., 1997. U–Pb dating on single detrital
501 zircon grains from the Triassic Songpan–Ganze flysch (Central China): provenance and
502 tectonic correlations. *Earth and Planetary Science Letters*, 152, 217-231.

503

504 6. Brown, L.D., Zhao, W., Nelson, K.D. and Hauck, M., 1996. Bright spots, structure, and
505 magmatism in southern Tibet from INDEPTH seismic reflection profiling. *Science*, 274, 1688.

506

- 507 7. Burchfiel, B.C., Molnar, P., Ziyun, Z., K'uangyi, L., Shuji, W., Minmin, H. and Sutter, J.,
508 1989. Geology of the Ulugh Muztagh area, northern Tibet. *Earth and Planetary Science*
509 *Letters*, 94, 57-70.
- 510
- 511 8. Cai, H., Zhang, H. and Xu, W., 2009. U-Pb zircon ages, geochemical and Sr-Nd-Hf
512 isotopic compositions of granitoids in western Songpan-Ganze fold belt: Petrogenesis and
513 implication for tectonic evolution. *Journal of Earth Science*, 20, 681-698.
- 514
- 515 9. Cai, H., Zhang, H., Xu, W., Shi, Z. and Yuan, H., 2010. Petrogenesis of Indosinian
516 volcanic rocks in Songpan-Ganze fold belt of the northeastern Tibetan Plateau: New
517 evidence for lithospheric delamination. *Science China Earth Sciences*, 53, 1316-1328.
- 518
- 519 10. Chen, L., Booker, J.R., Jones, A.G. and Wu, N., 1996. Electrically conductive crust in
520 Southern Tibet from INDEPTH magnetotelluric surveying. *Science*, 274, 1694.
- 521
- 522 11. Chen, Q., Sun, M., Long, X. and Yuan, C., 2015. Petrogenesis of Neoproterozoic
523 adakitic tonalites and high-K granites in the eastern Songpan-Ganze Fold Belt and
524 implications for the tectonic evolution of the western Yangtze Block. *Precambrian*
525 *Research*, 270, 181-203.
- 526
- 527 12. Chen, Y., Liu, F., Zhang, H., Nie, L. and Jiang, L., 2007. Elemental and Sm-Nd isotopic
528 geochemistry on detrital sedimentary rocks in the Ganzi-Songpan block and Longmen
529 Mountains. *Frontiers of Earth Science in China*, 1, 60-68.
- 530
- 531 13. Chen, Z., Liu, Y., Hodges, K.V., Burchfiel, B.C., Royden, L.H. and Deng, C., 1990. The
532 Kangmar Dome: a metamorphic core complex in southern Xizang (Tibet). *Science*, 250,
533 1552-1557.
- 534
- 535 14. Chen, Y., Luo, Z., Zhao, J., Li, Z., Zhang, H. and Song, B., 2005. Petrogenesis and
536 dating of the Kangding complex, Sichuan Province. *Science in China Series D: Earth Sciences*,
537 48(5), pp.622-634.
- 538

- 539 15. Chen, S.H.E., Wilson, C.J. and Worley, B.A., 1995. Tectonic transition from the
540 Songpan - Garzê Fold Belt to the Sichuan Basin, south - western China. *Basin Research*, 7,
541 235-253.
542
- 543 16. Chung, S.L., Chu, M.F., Zhang, Y., Xie, Y., Lo, C.H., Lee, T.Y., Lan, C.Y., Li, X., Zhang, Q.
544 and Wang, Y., 2005. Tibetan tectonic evolution inferred from spatial and temporal
545 variations in post-collisional magmatism. *Earth-Science Reviews*, 68, 173-196.
546
- 547 17. Clark, M.K., House, M.A., Royden, L.H., Whipple, K.X., Burchfiel, B.C., Zhang, X. and
548 Tang, W., 2005. Late Cenozoic uplift of southeastern Tibet. *Geology*, 33, 525-528.
549
- 550 18. Clark, M.K. and Royden, L.H., 2000. Topographic ooze: Building the eastern margin
551 of Tibet by lower crustal flow. *Geology*, 28, 703-706.
552
- 553 19. Cottle, J.M., Larson, K.P. and Kellett, D.A., 2015. How does the mid-crust
554 accommodate deformation in large, hot collisional orogens? A review of recent research in
555 the Himalayan orogen. *Journal of Structural Geology*, 78, 119-133.
556
- 557 20. Craig, T.J., Copley, A. and Jackson, J. 2012. Thermal and tectonic consequences of
558 India underthrusting Tibet. *Earth and Planetary Science Letters*, 353-354, 231-239.
559
- 560 21. de Sigoyer, J., Vanderhaeghe, O., Duchêne, S. and Billerot, A., 2014. Generation and
561 emplacement of Triassic granitoids within the Songpan Ganze accretionary-orogenic wedge
562 in a context of slab retreat accommodated by tear faulting, Eastern Tibetan plateau, China.
563 *Journal of Asian Earth Sciences*, 88, 192-216.
564
- 565 22. Decelles, P.G., Kapp, P., Gehrels, G.E. and Ding, L., 2014. Paleocene - Eocene
566 foreland basin evolution in the Himalaya of southern Tibet and Nepal: Implications for the
567 age of initial India - Asia collision. *Tectonics*, 33, 824-849.
568

- 569 23. Ding, L., Yang, D., Cai, F.L., Pullen, A., Kapp, P., Gehrels, G.E., Zhang, L.Y., Zhang,
570 Q.H., Lai, Q.Z., Yue, Y.H. and Shi, R.D., 2013. Provenance analysis of the Mesozoic Hoh - Xil
571 - Songpan - Ganzi turbidites in northern Tibet: Implications for the tectonic evolution of
572 the eastern Paleo - Tethys Ocean. *Tectonics*, 32, 34-48.
- 573
- 574 24. Enkelmann, E., Weislogel, A., Ratschbacher, L., Eide, E., Renno, A. and Wooden, J.,
575 2007. How was the Triassic Songpan - Ganzi basin filled? A provenance study. *Tectonics*,
576 26.
- 577
- 578 25. Fisher, C.M., Hanchar, J.M., Samson, S.D., Dhuime, B., Blichert-Toft, J., Vervoort, J.D.
579 and Lam, R., 2011. Synthetic zircon doped with hafnium and rare earth elements: a
580 reference material for in situ hafnium isotope analysis. *Chemical Geology*, 286, 32-47.
- 581
- 582 26. Gaillard, F., Scaillet, B. and Pichavant, M., 2004. Evidence for present-day
583 leucogranite pluton growth in Tibet. *Geology*, 32, 801-804.
- 584
- 585 27. Gehrels, G., Kapp, P., DeCelles, P., Pullen, A., Blakey, R., Weislogel, A., Ding, L.,
586 Guynn, J., Martin, A., McQuarrie, N. and Yin, A., 2011. Detrital zircon geochronology of pre
587 - Tertiary strata in the Tibetan - Himalayan orogen. *Tectonics*, 30.
- 588
- 589 28. Green, O.R., Searle, M.P., Corfield, R.I. and Corfield, R.M. 2008. Cretaceous-Tertiary
590 carbonate platform evolution and the age of the India-Asia collision along the Ladakh
591 Himalaya (Northwest India). *Journal of Geology*, 116, 331-353.
- 592
- 593 29. Griffin, W.L., Wang, X., Jackson, S.E., Pearson, N.J., O'Reilly, S.Y., Xu, X. and Zhou, X.,
594 2002. Zircon chemistry and magma mixing, SE China: in-situ analysis of Hf isotopes, Tonglu
595 and Pingtan igneous complexes. *Lithos*, 61, 237-269.
- 596
- 597 30. Grujic, D., Hollister, L.S. and Parrish, R.R., 2002. Himalayan metamorphic sequence
598 as an orogenic channel: insight from Bhutan. *Earth and Planetary Science Letters*, 198, 177-
599 191.

600

601 31. Guo, Z., Wilson, M., Liu, J. and Mao, Q., 2006. Post-collisional, potassic and
602 ultrapotassic magmatism of the northern Tibetan Plateau: Constraints on characteristics of
603 the mantle source, geodynamic setting and uplift mechanisms. *Journal of Petrology*, 47,
604 1177-1220.

605

606 32. Harrison, T.M., Copeland, P., Kidd, W.S.F. and Lovera, O.M., 1995. Activation of the
607 Nyainqentanghla shear zone: Implications for uplift of the southern Tibetan Plateau.
608 *Tectonics*, 14, 658-676.

609

610 33. Harrowfield, M.J. and Wilson, C.J., 2005. Indosinian deformation of the Songpan
611 Ganze fold belt, northeast Tibetan Plateau. *Journal of Structural Geology*, 27, 101-117.

612

613 34. Hodges, K.V., 2000. Tectonics of the Himalaya and southern Tibet from two
614 perspectives. *Geological Society of America Bulletin*, 112, 324-350.

615

616 35. Hollister, L.S. and Crawford, M.L., 1986. Melt-enhanced deformation: A major
617 tectonic process. *Geology*, 14, 558-561.

618

619 36. Hou, Z.Q., Zheng, Y.C., Zeng, L.S., Gao, L.E., Huang, K.X., Li, W., Li, Q.Y., Fu, Q., Liang,
620 W. and Sun, Q.Z., 2012. Eocene–Oligocene granitoids in southern Tibet: constraints on
621 crustal anatexis and tectonic evolution of the Himalayan orogen. *Earth and Planetary
622 Science Letters*, 349, 38-52.

623

624 37. Hu, X., Garzanti, E., Wang, J., Huang, W., An, W. and Webb, A., 2016. The timing of
625 India-Asia collision onset—Facts, theories, controversies. *Earth-Science Reviews*, 160, 264-
626 299.

627

628 38. Huang, M.H., Buick, I.S. and Hou, L.W., 2003a. Tectonometamorphic evolution of
629 the eastern Tibet plateau: Evidence from the central Songpan–Garzê orogenic belt,
630 Western China. *Journal of Petrology*, 44, 255-278.

631

- 632 39. Huang, M., Maas, R., Buick, I.S. and Williams, I.S., 2003b. Crustal response to
633 continental collisions between the Tibet, Indian, South China and North China blocks:
634 Geochronological constraints from the Songpan - Ganze orogenic belt, western China.
635 *Journal of Metamorphic Geology*, 21, 223-240.
- 636
- 637 40. Hubbard, J. and Shaw, J.H., 2009. Uplift of the Longmen Shan and Tibetan plateau,
638 and the 2008 Wenchuan (M= 7.9) earthquake. *Nature*, 458, 194-197.
- 639
- 640 41. Hubbard, J., Shaw, J.H. and Klinger, Y., 2010. Structural setting of the 2008 Mw 7.9
641 Wenchuan, China, earthquake. *Bulletin of the Seismological Society of America*, 100(5B),
642 pp.2713-2735.
- 643
- 644 42. Jamieson, R.A., Unsworth, M.J., Harris, N.B., Rosenberg, C.L. and Schulmann, K.,
645 2011. Crustal melting and the flow of mountains. *Elements*, 7(4), pp.253-260.
- 646
- 647 43. Kapp, J.L.A., Harrison, T.M., Kapp, P., Grove, M., Lovera, O.M. and Lin, D., 2005.
648 Nyainqentanglha Shan: a window into the tectonic, thermal, and geochemical evolution of
649 the Lhasa block, southern Tibet. *Journal of Geophysical Research: Solid Earth*, 110(B8).
- 650
- 651 44. Kapp, P., Taylor, M., Stockli, D. and Ding, L., 2008. Development of active low-angle
652 normal fault systems during orogenic collapse: Insight from Tibet. *Geology*, 36, 7-10.
- 653
- 654 45. King, J., Harris, N., Argles, T., Parrish, R. and Zhang, H., 2011. Contribution of crustal
655 anatexis to the tectonic evolution of Indian crust beneath southern Tibet. *Geological
656 Society of America Bulletin*, 123, 218-239.
- 657
- 658 46. Lai, Q., Ding, L., Wang, H., Yue, Y. and Cai, F., 2007. Constraining the stepwise
659 migration of the eastern Tibetan Plateau margin by apatite fission track thermochronology.
660 *Science in China Series D: Earth Sciences*, 50, 172-183.
- 661

- 662 47. Laskowski, A.K., Kapp, P., Ding, L., Campbell, C. Liu, X. 2016. Tectonic evolution of
663 the Yarlung suture zone, Lopu Range region, southern Tibet. *Tectonics*, 36, 108,
664 doi:10.1002/2016TC004334.
665
- 666 48. Li, H. and Zhang, Y., 2013. Zircon U–Pb geochronology of the Konggar granitoid and
667 migmatite: Constraints on the Oligo-Miocene tectono-thermal evolution of the Xianshuihe
668 fault zone, East Tibet. *Tectonophysics*, 606, 127-139.
669
- 670 49. Li, H., Zhang, Y., Zhang, C., Dong, S. and Zhu, F., 2015. Middle Jurassic syn-kinematic
671 magmatism, anatexis and metamorphism in the Zheduo-Gonggar massif, implication for
672 the deformation of the Xianshuihe fault zone, East Tibet. *Journal of Asian Earth Sciences*,
673 107, 35-52.
674
- 675 50. Li, S., Unsworth, M.J., Booker, J.R., Wei, W., Tan, H. and Jones, A.G., 2003. Partial
676 melt or aqueous fluid in the mid-crust of Southern Tibet? Constraints from INDEPTH
677 magnetotelluric data. *Geophysical Journal International*, 153, 289-304.
678
- 679 51. Li, Y., Jia, D., Shaw, J.H., Hubbard, J., Lin, A., Wang, M., Luo, L., Li, H. and Wu, L.,
680 2010. Structural interpretation of the coseismic faults of the Wenchuan earthquake: Three
681 - dimensional modeling of the Longmen Shan fold - and - thrust belt. *Journal of*
682 *Geophysical Research: Solid Earth*, 115, .
683
- 684 52. Li, Y., Jia, D., Wang, M., Shaw, J.H., He, J., Lin, A., Xiong, L. and Rao, G., 2014.
685 Structural geometry of the source region for the 2013 Mw 6.6 Lushan earthquake:
686 Implication for earthquake hazard assessment along the Longmen Shan. *Earth and*
687 *Planetary Science Letters*, 390, 275-286.
688
- 689 53. Liu, S.W., Wang, Z.Q., Yan, Q.R., Li, Q.G., Zhang, D.H. and Wang, J.G., 2006. Timing,
690 petrogenesis and geodynamic significance of Zheduoshan Granitoids. *Acta Petrologica*
691 *Sinica*, 22, 343-352.
692

- 693 54. Liu, Q., Wu, Z., Hu, D., Ye, P., Jiang, W., Wang, Y. and Zhang, H., 2004. SHRIMP U-Pb
694 zircon dating on Nyainqentanglha granite in central Lhasa block. *Chinese Science Bulletin*,
695 49, 76-82.
- 696
- 697 55. Makovsky, Y. and Klemperer, S.L., 1999. Measuring the seismic properties of Tibetan
698 bright spots: Evidence for free aqueous fluids in the Tibetan middle crust. *Journal of*
699 *Geophysical Research: Solid Earth*, 104, 10795-10825.
- 700
- 701 56. Makovsky, Y., Klemperer, S.L., Ratschbacher, L., Brown, L.D., Li, M., Zhao, W. and
702 Meng, F., 1996. INDEPTH wide-angle reflection observation of P-wave-to-S-wave
703 conversion from crustal bright spots in Tibet. *Science*, 274, 1690-1692.
- 704
- 705 57. Miller, C., Schuster, R., Klötzli, U., Frank, W. and Purtscheller, F., 1999. Post-
706 collisional potassic and ultrapotassic magmatism in SW Tibet: geochemical and Sr-Nd-Pb-
707 O isotopic constraints for mantle source characteristics and petrogenesis. *Journal of*
708 *Petrology*, 40, 1399-1424.
- 709
- 710 58. Nabelek, J., Hétenyi, G., Vergne, J., et al. 2009. Underplating in the Himalaya-Tibet
711 collision zone revealed by the Hi-CLIMB Experiment. *Science*, 325, 1371-1374.
- 712
- 713 59. Najman, Y., Appel, E., Boudagher - Fadel, M., Bown, P., Carter, A., Garzanti, E.,
714 Godin, L., Han, J., Liebke, U., Oliver, G. and Parrish, R., 2010. Timing of India - Asia collision:
715 Geological, biostratigraphic, and palaeomagnetic constraints. *Journal of Geophysical*
716 *Research: Solid Earth*, 115(B12).
- 717
- 718 60. Najman, Y., Jenks, D., Godin, L., Boudagher-Fadel, M., Millar, I., Garzanti, E.,
719 Horstwood, M. and Bracciali, L., 2017. The Tethyan Himalayan detrital record shows that
720 India-Asia terminal collision occurred by 54 Ma in the Western Himalaya. *Earth and*
721 *Planetary Science Letters*, 459, 301-310.
- 722

- 723 61. Nelson, K.D., Zhao, W., Brown, L.D. and Kuo, J., 1996. Partially molten middle crust
724 beneath southern Tibet: synthesis of project INDEPTH results. *Science*, 274, 1684.
725
- 726 62. Prestley, K., Jackson, J. and McKenzie, D. 2008. Lithospheric structure and deep
727 earthquakes beneath India, the Himalaya and southern Tibet. *Geophysical Journal*
728 *International*, 172, 345-362.
729
- 730 63. Roger, F., Calassou, S., Lancelot, J., Malavieille, J., Mattauer, M., Zhiqin, X., Ziwen, H.
731 and Liwei, H., 1995. Miocene emplacement and deformation of the Konga Shan granite
732 (Xianshui He fault zone, west Sichuan, China): Geodynamic implications. *Earth and*
733 *Planetary Science Letters*, 130, 201-216.
734
- 735 64. Roger, F., Jolivet, M. and Malavieille, J., 2010. The tectonic evolution of the
736 Songpan-Garzê (North Tibet) and adjacent areas from Proterozoic to Present: A synthesis.
737 *Journal of Asian Earth Sciences*, 39, 254-269.
738
- 739 65. Roger, F., Malavieille, J., Leloup, P.H., Calassou, S. and Xu, Z., 2004. Timing of granite
740 emplacement and cooling in the Songpan–Garzê Fold Belt (eastern Tibetan Plateau) with
741 tectonic implications. *Journal of Asian Earth Sciences*, 22, 465-481.
742
- 743 66. Rosenberg, C.L. and Handy, M.R., 2005. Experimental deformation of partially
744 melted granite revisited: implications for the continental crust. *Journal of metamorphic*
745 *Geology*, 23, 19-28.
746
- 747 67. Royden, L.H., Burchfiel, B.C., King, R.W., Wang, E., Chen, Z., Shen, F. and Liu, Y.,
748 1997. Surface deformation and lower crustal flow in eastern Tibet. *science*, 276, 788-790.
749
- 750 68. Searle, M.P., Cottle, J.M., Streule, M.J. and Waters, D.J., 2010. Crustal melt granites
751 and migmatites along the Himalaya: melt source, segregation, transport and granite
752 emplacement mechanisms. *Geological Society of America Special Papers*, 472, 219-233
753

- 754 69. Searle, M.P., Elliott, J.R., Phillips, R.J. and Chung, S-L. 2011. Crustal – lithospheric
755 structure and continental extrusion of Tibet. *Journal of the Geological Society, London*, 168,
756 633-672, doi: 10.1144/0016-76492010-139
757
- 758 70. Searle, M.P., Law, R.D. and Jessup, M.J., 2006. Crustal structure, restoration and
759 evolution of the Greater Himalaya in Nepal-South Tibet: implications for channel flow and
760 ductile extrusion of the middle crust. *Geological Society, London, Special Publications*, 268,
761 355-378.
762
- 763 71. Searle, M.P., Roberts, N.M., Chung, S.L., Lee, Y.H., Cook, K.L., Elliott, J.R., Weller,
764 O.M., St-Onge, M.R., Xu, X.W., Tan, X.B. and Li, K., 2016. Age and anatomy of the Gongga
765 Shan batholith, eastern Tibetan Plateau, and its relationship to the active Xianshui-he fault.
766 *Geosphere*, 12, 948-970.
767
- 768 72. Sláma, J. et al., 2008. Plešovice zircon—a new natural reference material for U–Pb
769 and Hf isotopic microanalysis. *Chemical Geology* 249, 1-35.
770
- 771 73. Söderlund, U., Patchett, P.J., Vervoort, J.D. and Isachsen, C.E., 2004. The 176 Lu
772 decay constant determined by Lu–Hf and U–Pb isotope systematics of Precambrian mafic
773 intrusions. *Earth and Planetary Science Letters*, 219, 311-324.
774
- 775 74. Spencer, C.J., Cawood, P.A., Hawkesworth, C.J., Prave, A.R., Roberts, N.M.,
776 Horstwood, M.S. and Whitehouse, M.J., 2015. Generation and preservation of continental
777 crust in the Grenville Orogeny. *Geoscience Frontiers*, 6, 357-372.
778
- 779 75. Streule, M.J., Searle, M.P., Waters, D.J. and Horstwood, M.S., 2010. Metamorphism,
780 melting, and channel flow in the Greater Himalayan Sequence and Makalu leucogranite:
781 Constraints from thermobarometry, metamorphic modeling, and U - Pb geochronology.
782 *Tectonics*, 29, TC5011, doi: 10,1029/2009TC002533
783

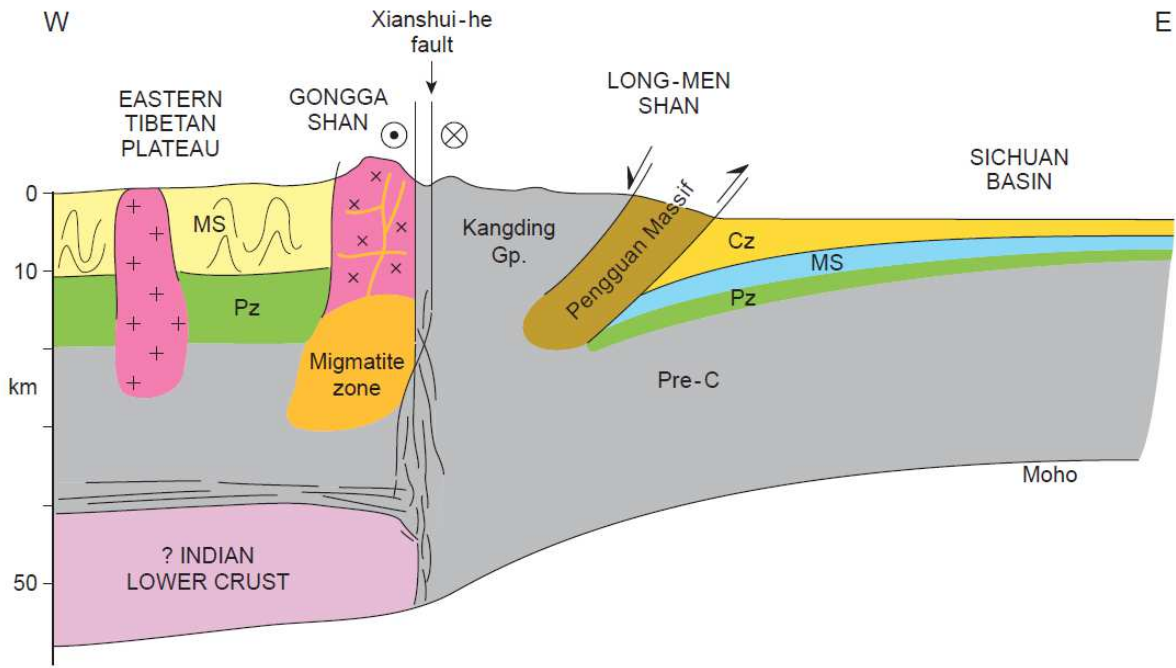
- 784 76. Unsworth, M.J., Jones, A.G., Wei, W., Marquis, G., Gokarn, S.G., Spratt, J.E.,
785 Bedrosian, P., Booker, J., Leshou, C., Clarke, G. and Shenghui, L., 2005. Crustal rheology of
786 the Himalaya and Southern Tibet inferred from magnetotelluric data. *Nature*, *438*, 78-81.
787
- 788 77. Wang, Z., Huang, R. and Pei, S., 2014. Crustal deformation along the Longmen-Shan
789 fault zone and its implications for seismogenesis. *Tectonophysics*, *610*, 128-137.
790
- 791 78. Wang, W., Liu, S., Feng, Y., Li, Q., Wu, F., Wang, Z., Wang, R. and Yang, P., 2012.
792 Chronology, petrogenesis and tectonic setting of the Neoproterozoic Tongchang dioritic
793 pluton at the northwestern margin of the Yangtze Block: constraints from geochemistry
794 and zircon U–Pb–Hf isotopic systematics. *Gondwana Research*, *22*, 699-716.
795
- 796 79. Wei, W., Unsworth, M., Jones, A., Booker, J., Tan, H., Nelson, D., Chen, L., Li, S.,
797 Solon, K., Bedrosian, P. and Jin, S., 2001. Detection of widespread fluids in the Tibetan crust
798 by magnetotelluric studies. *Science*, *292*, 716-719.
799
- 800 80. Weislogel, A.L., 2008. Tectonostratigraphic and geochronologic constraints on
801 evolution of the northeast Paleotethys from the Songpan-Ganzi complex, central China.
802 *Tectonophysics*, *451*(1), pp.331-345.
803
- 804 81. Weislogel, A.L., Graham, S.A., Chang, E.Z., Wooden, J.L., Gehrels, G.E. and Yang, H.,
805 2006. Detrital zircon provenance of the Late Triassic Songpan-Ganzi complex: Sedimentary
806 record of collision of the North and South China blocks. *Geology*, *34*, 97-100.
807
- 808 82. Weislogel, A.L., Graham, S.A., Chang, E.Z., Wooden, J.L. and Gehrels, G.E., 2010.
809 Detrital zircon provenance from three turbidite depocenters of the Middle–Upper Triassic
810 Songpan-Ganzi complex, central China: Record of collisional tectonics, erosional
811 exhumation, and sediment production. *Geological Society of America Bulletin*, *122*, 2041-
812 2062.
813
- 814 83. Weller, O.M., St-Onge, M.R., Waters, D.J., Rayner, N., Searle, M.P., Chung, S-L.,
815 Palin, R.M., Lee, Y-H., and Xu, X. 2013. Quantifying Barrovian metamorphism in the Danba

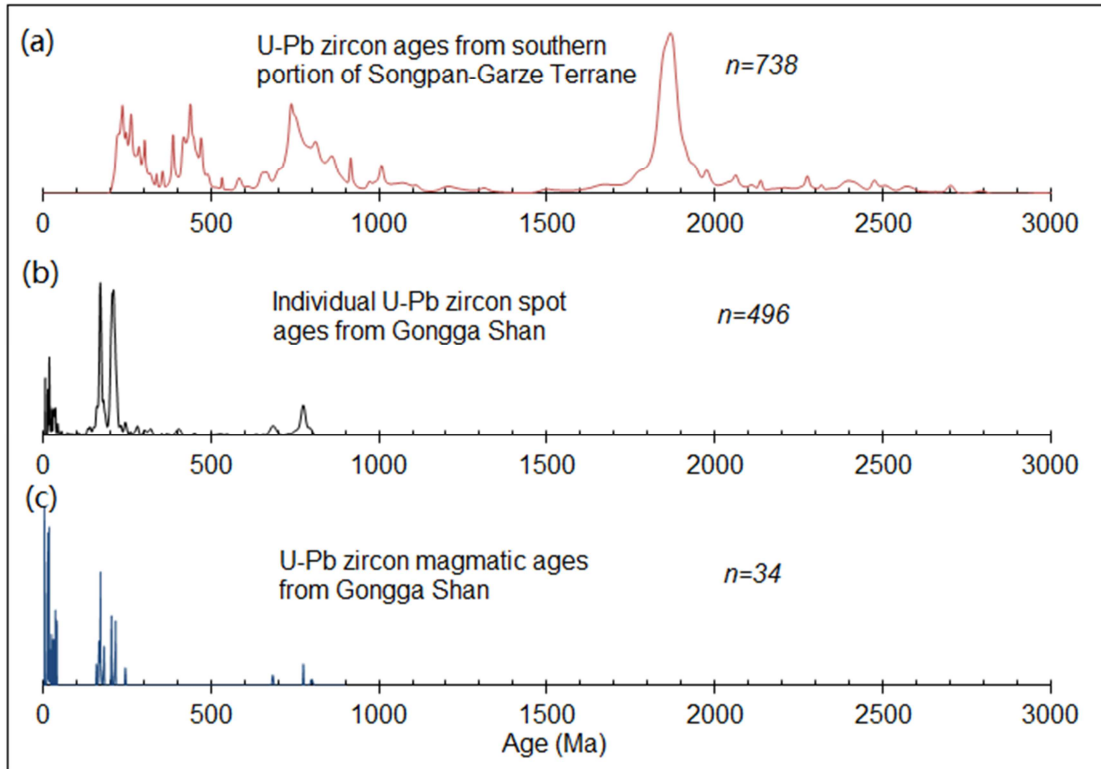
- 816 structural culmination of eastern Tibet. *Journal of Metamorphic Geology*,
817 doi:10.1111/jmg.12050
818
- 819 84. Weller, O.M., St-Onge, M.R., Rayner, N., Searle, M.P. and Waters, D.J., 2016.
820 Miocene magmatism in the Western Nyainqentanglha mountains of southern Tibet: An
821 exhumed bright spot?. *Lithos*, 245, 147-160.
822
- 823 85. Wiedenbeck, M. A. P. C. et al., 1995. Three natural zircon standards for U - Th - Pb,
824 Lu - Hf, trace element and REE analyses. *Geostandards newsletter* 19, 1-23.
825
- 826 86. Wiedenbeck, M.A.P.C. et al., 2004. Further characterisation of the 91500 Zircon
827 Crystal. *Geostandards and Geoanalytical Research* 28, 9-39.
828
- 829 87. Williams, H.M., Turner, S.P., Pearce, J.A., Kelley, S.P. and Harris, N.B.W., 2004.
830 Nature of the source regions for post-collisional, potassic magmatism in southern and
831 northern Tibet from geochemical variations and inverse trace element modelling. *Journal of*
832 *Petrology*, 45, 555-607.
833
- 834 88. Xiao, L., Zhang, H.F., Clemens, J.D., Wang, Q.W., Kan, Z.Z., Wang, K.M., Ni, P.Z. and
835 Liu, X.M., 2007. Late Triassic granitoids of the eastern margin of the Tibetan Plateau:
836 geochronology, petrogenesis and implications for tectonic evolution. *Lithos*, 96, 436-452.
837
- 838 89. Xu, R.H., Schärer, U. and Allègre, C.J., 1985. Magmatism and metamorphism in the
839 Lhasa block (Tibet): a geochronological study. *The Journal of Geology*, 93, 41-57.
840
- 841 90. Yuan, C., Zhou, M.F., Sun, M., Zhao, Y., Wilde, S., Long, X. and Yan, D., 2010. Triassic
842 granitoids in the eastern Songpan Ganzi Fold Belt, SW China: magmatic response to
843 geodynamics of the deep lithosphere. *Earth and Planetary Science Letters*, 290, 481-492.
844

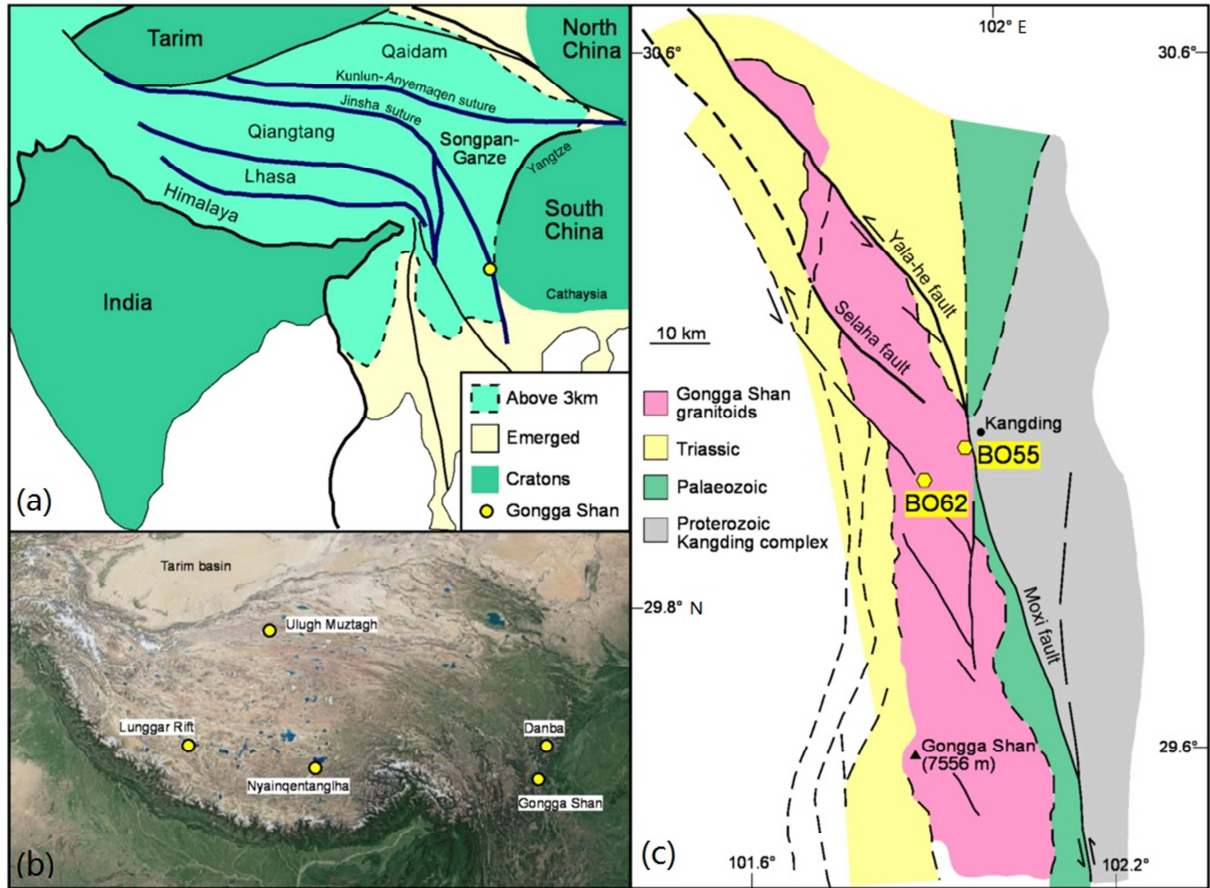
- 845 91. Zeng, L., Gao, L.E., Xie, K. and Liu-Zeng, J., 2011. Mid-Eocene high Sr/Y granites in
846 the Northern Himalayan Gneiss Domes: melting thickened lower continental crust. *Earth
847 and Planetary Science Letters*, 303, 251-266.
- 848
- 849 92. Zhang, H.F., Parrish, R., Zhang, L., Xu, W.C., Yuan, H.L., Gao, S. and Crowley, Q.G.,
850 2007. A-type granite and adakitic magmatism association in Songpan–Ganze fold belt,
851 eastern Tibetan Plateau: implication for lithospheric delamination. *Lithos*, 97, 323-335.
- 852
- 853 93. Zhang, H.F., Zhang, L., Harris, N., Jin, L.L. and Yuan, H., 2006. U–Pb zircon ages,
854 geochemical and isotopic compositions of granitoids in Songpan–Ganze fold belt, eastern
855 Tibetan Plateau: constraints on petrogenesis and tectonic evolution of the basement.
856 *Contributions to Mineralogy and Petrology*, 152(1), pp.75-88.
- 857
- 858 94. Zhang, Y.X., Tang, X.C., Zhang, K.J., Zeng, L. and Gao, C.L., 2014. U–Pb and Lu–Hf
859 isotope systematics of detrital zircons from the Songpan–Ganzi Triassic flysch, NE Tibetan
860 Plateau: Implications for provenance and crustal growth. *International Geology Review*, 56,
861 29-56.
- 862
- 863 95. Zhang, Y.X., Zeng, L., Li, Z.W., Wang, C.S., Zhang, K.J., Yang, W.G. and Guo, T.L.,
864 2015. Late Permian–Triassic siliciclastic provenance, palaeogeography, and crustal growth
865 of the Songpan terrane, eastern Tibetan Plateau: evidence from U–Pb ages, trace elements,
866 and Hf isotopes of detrital zircons. *International Geology Review*, 57, 159-181.
- 867
- 868 96. Zhang, Y.Z., Replumaz, A., Leloup, P.H., Wang, G.C., Bernet, M., van der Beek, P.,
869 Paquette, J.L. and Chevalier, M.L., 2017. Cooling history of the Gongga batholith:
870 Implications for the Xianshuihe Fault and Miocene kinematics of SE Tibet. *Earth and
871 Planetary Science Letters*, 465, 1-15.
- 872
- 873 97. Zhao, J.H. and Zhou, M.F., 2007a. Geochemistry of Neoproterozoic mafic intrusions
874 in the Panzihua district (Sichuan Province, SW China): implications for subduction-related
875 metasomatism in the upper mantle. *Precambrian Research*, 152, 27-47.
- 876

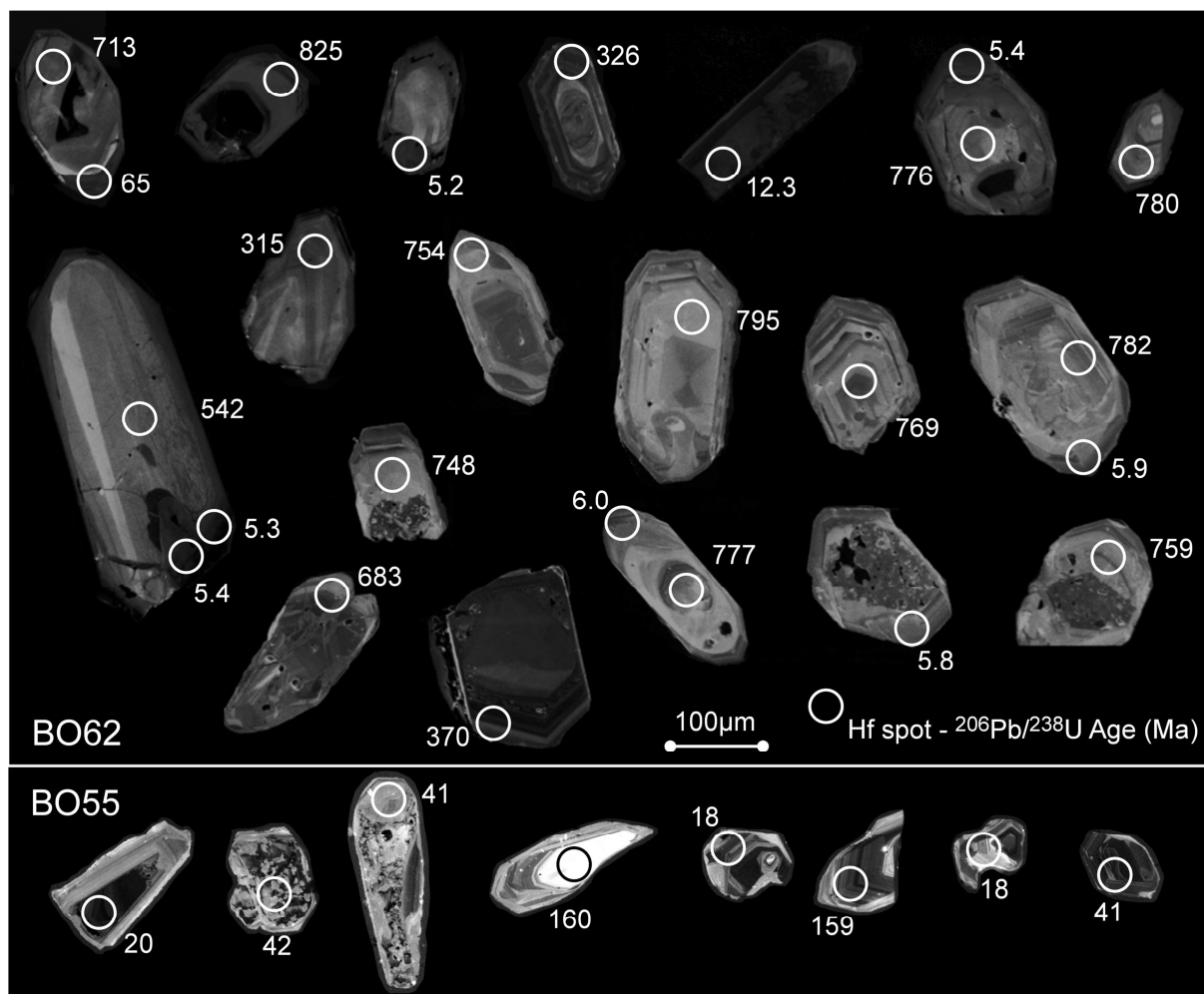
- 877 98. Zhao, J.H. and Zhou, M.F., 2007b. Neoproterozoic adakitic plutons and arc
878 magmatism along the western margin of the Yangtze Block, South China. *The Journal of*
879 *Geology*, 115, 675-689.
- 880
- 881 99. Zhao, J.H., Zhou, M.F., Yan, D.P., Yang, Y.H. and Sun, M., 2008a. Zircon Lu–Hf
882 isotopic constraints on Neoproterozoic subduction-related crustal growth along the
883 western margin of the Yangtze Block, South China. *Precambrian Research*, 163, 189-209.
- 884
- 885 100. Zhao, X.F., Zhou, M.F., Li, J.W. and Wu, F.Y., 2008b. Association of Neoproterozoic
886 A- and I-type granites in South China: implications for generation of A-type granites in a
887 subduction-related environment. *Chemical Geology*, 257(1), pp.1-15.
- 888
- 889 101. Zheng, Y.F., Zhang, S.B., Zhao, Z.F., Wu, Y.B., Li, X., Li, Z. and Wu, F.Y., 2007.
890 Contrasting zircon Hf and O isotopes in the two episodes of Neoproterozoic granitoids in
891 South China: implications for growth and reworking of continental crust. *Lithos*, 96, 127-
892 150.
- 893
- 894 102. Zhou, M.F., Yan, D.P., Kennedy, A.K., Li, Y. and Ding, J., 2002. SHRIMP U–Pb zircon
895 geochronological and geochemical evidence for Neoproterozoic arc-magmatism along the
896 western margin of the Yangtze Block, South China. *Earth and Planetary Science Letters*,
897 196(1), pp.51-67.

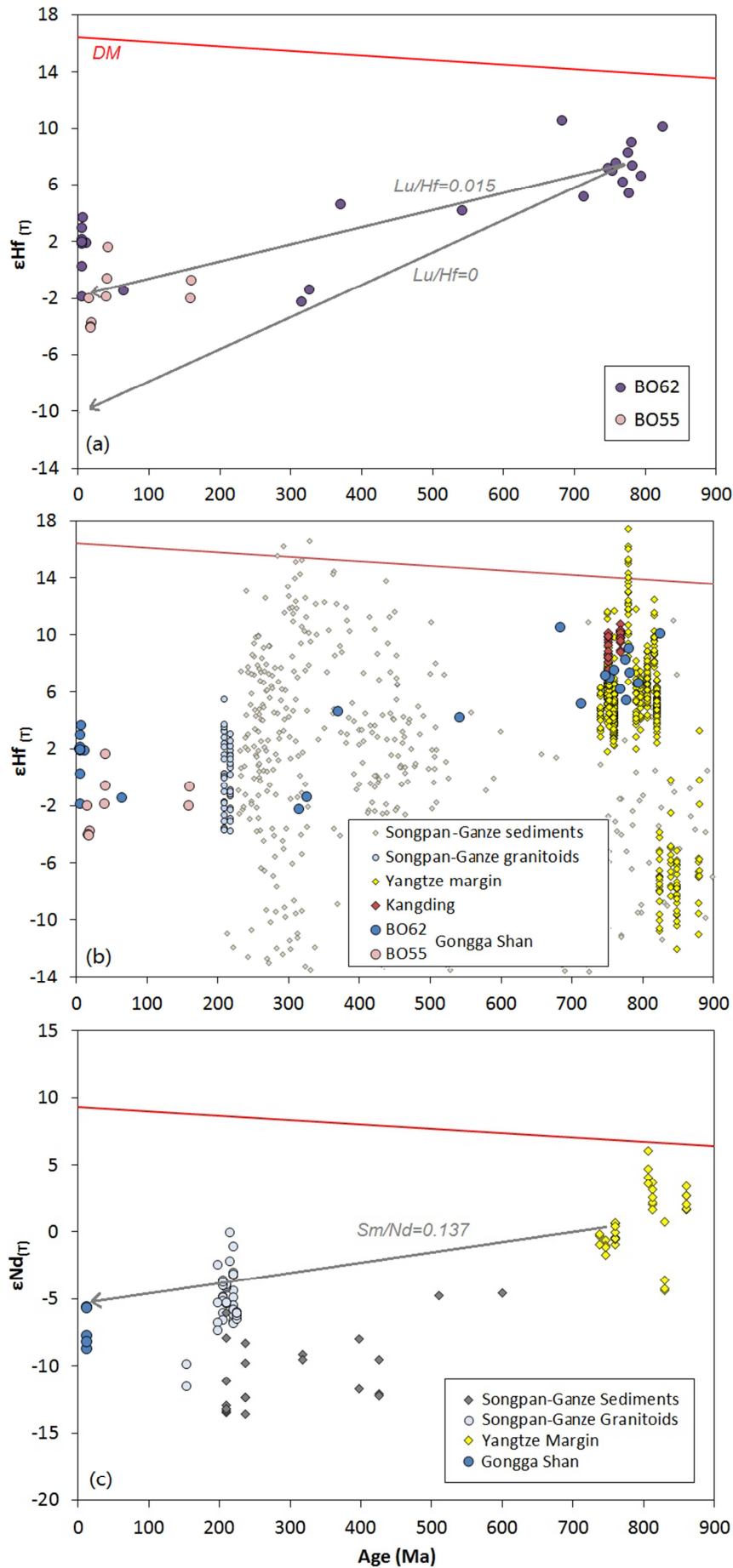
Sample	Spot	Age (Ma)		Age (Ma)		Total Hf (V)	$^{180}\text{Hf}/^{177}\text{Hf}$		$^{176}\text{Yb}/^{177}\text{Hf}$		$^{176}\text{Lu}/^{177}\text{Hf}$		$^{176}\text{Hf}/^{177}\text{Hf}$		$\epsilon_{\text{Hf}}(t)$	
		$^{207}\text{Pb}/^{206}\text{Pb}$	2 σ	$^{206}\text{Pb}/^{238}\text{U}$	2 σ		2 σ	2 σ	2 σ	2 σ	2 σ	2 σ	2 σ	2 σ		
BO52	B_01	132.4	36.5	15.2	0.5	10	1.886484	0.000146	0.026015	0.001795	0.000985	0.000108	0.282719	0.000036	-2.02	1.28
BO52	B_02	-18.9	26.8	41.9	0.9	32	1.886733	0.000078	0.029254	0.001202	0.000879	0.000018	0.282805	0.000031	1.60	1.08
BO52	B_03	34.7	24.8	40.5	1.1	19	1.886692	0.000090	0.021563	0.001452	0.000627	0.000008	0.282706	0.000032	-1.92	1.12
BO52	B_06	53.5	21.8	19.5	0.4	15	1.886763	0.000173	0.030188	0.003833	0.000816	0.000100	0.282667	0.000053	-3.76	1.87
BO52	B_08	156.9	44.5	160.2	4.4	14	1.886858	0.000123	0.021961	0.001273	0.000536	0.000045	0.282666	0.000033	-0.71	1.16
BO52	B_09	158.7	17.5	158.9	2.8	21	1.886717	0.000079	0.031845	0.001308	0.000833	0.000003	0.282631	0.000032	-2.01	1.14
BO52	B_10	57.0	24.9	17.5	0.4	13	1.886629	0.000166	0.036159	0.001287	0.000982	0.000070	0.282661	0.000048	-4.02	1.69
BO52	B_11	-16.8	31.3	17.6	0.4	18	1.886864	0.000102	0.023210	0.000821	0.000626	0.000021	0.282658	0.000031	-4.12	1.10
BO52	B_13	218.9	28.4	41.1	1.1	22	1.886846	0.000099	0.020255	0.001340	0.000608	0.000061	0.282743	0.000034	-0.60	1.20
BO62	B_01	638.1	44.6	64.5	3.2	22	1.886745	0.000087	0.012771	0.000327	0.000353	0.000006	0.282704	0.000031	-1.46	1.08
BO62	B_02	776.4	21.4	824.9	19.6	19	1.886803	0.000074	0.042714	0.001443	0.001095	0.000015	0.282565	0.000033	10.10	1.16
BO62	B_03	796.1	185.3	5.2	0.4	20	1.886774	0.000086	0.012101	0.000597	0.000330	0.000013	0.282838	0.000032	1.98	1.12
BO62	B_04	794.9	24.7	315.4	14.9	21	1.886731	0.000073	0.058623	0.001098	0.001693	0.000022	0.282533	0.000029	-2.25	1.03
BO62	B_08	275.4	99.1	5.4	0.3	21	1.886798	0.000097	0.015125	0.002364	0.000395	0.000052	0.282842	0.000029	2.12	1.03
BO62	B_09	161.7	81.1	5.3	0.2	25	1.886710	0.000086	0.020302	0.001316	0.000516	0.000033	0.282865	0.000032	2.93	1.12
BO62	B_15	-0.7	35.4	12.3	0.3	25	1.886850	0.000059	0.076630	0.002812	0.002317	0.000051	0.282831	0.000028	1.87	1.00
BO62	B_16	280.3	92.9	5.4	0.2	24	1.886802	0.000086	0.019170	0.000782	0.000498	0.000011	0.282789	0.000031	0.25	1.10
BO62	B_17	774.1	19.7	775.6	18.7	15	1.886776	0.000108	0.067250	0.001625	0.001871	0.000013	0.282555	0.000030	8.26	1.04
BO62	B_19	767.9	26.3	753.6	18.3	15	1.886798	0.000093	0.022109	0.001099	0.000649	0.000020	0.282515	0.000033	6.99	1.16
BO62	B_21	832.7	19.1	326.0	22.8	22	1.886860	0.000091	0.100611	0.001038	0.002733	0.000029	0.282556	0.000033	-1.44	1.18
BO62	B_22	850.3	22.1	794.5	17.6	15	1.886864	0.000082	0.037501	0.000279	0.000974	0.000008	0.282483	0.000032	6.59	1.12
BO62	B_25	507.3	110.7	5.8	0.3	25	1.886805	0.000071	0.013853	0.000404	0.000339	0.000003	0.282834	0.000030	1.85	1.06
BO62	C_01	748.4	24.1	713.8	16.8	21	1.886797	0.000099	0.028087	0.000717	0.000786	0.000028	0.282490	0.000029	5.16	1.01
BO62	C_02	740.4	23.9	780.8	19.5	18	1.886902	0.000073	0.045035	0.001092	0.001289	0.000015	0.282565	0.000030	9.03	1.04
BO62	C_04	716.7	98.3	541.9	28.6	17	1.886822	0.000094	0.009775	0.000560	0.000312	0.000011	0.282564	0.000031	4.17	1.08
BO62	C_11	364.4	173.3	5.9	0.4	18	1.886761	0.000100	0.020532	0.000838	0.000531	0.000018	0.282837	0.000031	1.96	1.08
BO62	C_12	799.4	20.7	783.3	16.1	16	1.886841	0.000085	0.086422	0.002572	0.002268	0.000009	0.282531	0.000030	7.37	1.04
BO62	C_14	799.4	19.6	769.7	13.5	18	1.886806	0.000072	0.093375	0.000976	0.002397	0.000035	0.282508	0.000032	6.20	1.14
BO62	C_15	797.9	23.2	760.5	17.6	18	1.886818	0.000101	0.045545	0.001967	0.001298	0.000028	0.282536	0.000030	7.56	1.04
BO62	C_17	780.1	25.1	778.3	18.7	19	1.886800	0.000126	0.082538	0.004518	0.002028	0.000054	0.282475	0.000031	5.40	1.10
BO62	C_19	1848.5	122.4	6.0	0.4	20	1.886766	0.000089	0.022793	0.001140	0.000581	0.000038	0.282728	0.000035	-1.90	1.23
BO62	C_21	766.7	28.3	370.7	11.9	28	1.886721	0.000074	0.023687	0.000162	0.000672	0.000016	0.282687	0.000029	4.63	1.01
BO62	C_36	814.6	20.1	750.3	15.4	20	1.886794	0.000081	0.045174	0.000227	0.001320	0.000023	0.282532	0.000031	7.18	1.08
BO62	C_39	827.1	123.1	7.0	0.5	22	1.886839	0.000072	0.017367	0.000245	0.000494	0.000004	0.282884	0.000034	3.64	1.20
BO62	C_40	744.7	34.5	685.3	15.5	16	1.886799	0.000076	0.022307	0.000780	0.000751	0.000020	0.282660	0.000032	10.57	1.14











CRIP

1. Neoproterozoic crust underlies Gongga Shan
2. Bright spots beneath Tibetan Plateau relates to localised melts
3. Dry granulites of the lower Indian crust were underthrust

ACCEPTED MANUSCRIPT